RSC Advances

PAPER

View Article Online
View Journal | View Issue

Cite this: *RSC Adv.*, 2025, **15**, 48862

Easy access to Fe_2N nanomaterials from Fe nanocrystals and investigation of their electrocatalytic properties for the water electrolysis and CO_2 reduction

Azadeh Edalat,[ab] Laure Vendier,[a] Catherine Amiens, *[a] Marc Respaud,[b] Pierre Roblin,[c] Jérôme Esvan,[d] Quyen T. Nguyen,[e] Duc N. Nguyen,[e] Vu T. Tran,[e] Ly T. Le,[e] Phong D. Tran *[e] and Frederic Dumestre[f]

The nanostructured iron nitride phases, comprising only non-toxic and abundant elements, show potential in a wide range of applications, and are thus of great interest in the context of sustainable development. Especially, the nanostructured ε-Fe_xN phase ($x = 2–3$) can play the role of electrocatalyst (in fuel cells or for hydrogen production), or of anode in Li-ion batteries. However, obtaining morphology and composition (x) controlled nanoparticles of this phase is challenging. Here we show that α-Fe nanoparticles produced by an organometallic approach can be nitridated by a simple exposure to an ammonia flow in mild conditions of temperature, either in the powder form or as thin layers on FTO electrodes while keeping their initial morphology. Structural and magnetic measurements, combined with chemical analysis, and spectroscopic investigations evidenced the formation of the pure ε-Fe_2N phase, with a preserved nanostructure. The electrocatalytic activity of this nanomaterial has been evaluated for CO_2 reduction and for the oxygen evolution reaction. These results may open new perspectives for studying the properties and reactivity of ε-Fe_2N nanomaterials, and promote their use.

Received 22nd October 2025
Accepted 27th November 2025

DOI: 10.1039/d5ra08111d

rsc.li/rsc-advances

1. Introduction

Iron nitrides which combine the abundant and environmentally friendly Fe and N elements are attractive materials in the context of the growing demand for sustainable and greener technologies. In the past ten years, nanostructured iron nitride materials of various compositions and structures have been reported in the literature. Depending on the phase formed, many applications have been envisaged.[1–3] For example, the ε phase exists for compositions between Fe_3N and Fe_2N, with a magnetization that decreases continuously when the N content increases in the material.[4] Accordingly, ε-Fe_3N nanoparticles (NPs) have been envisaged for biomedical applications thanks to their interesting magnetic properties.[5,6] Meanwhile ε-Fe_2N nanomaterials are particularly interesting in electrocatalytic applications as electrocatalyst for the water splitting,[7,8] in proton exchange membrane fuel cell,[9–12] or in energy storage devices.[13] It makes them promising materials to promote a decarbonated industry.

The water splitting, being a key chemical process for the green H_2 production technology, is constituted of coupled two half redox reactions, namely the hydrogen evolution reaction (HER) and the oxygen evolution reaction (OER), the latter being the most challenging to efficiently catalyze. Noble-metal-based electrocatalysts such as IrO_2 NPs, RuO_2 NPs are the best OER catalysts for instance. However, the limited abundance of noble metals motivates scientists to search for alternatives which are made of earth-abundant-elements.[14–16] Nitrides of first-rows transition metals have been synthesized and demonstrated to be promising alternative OER catalysts,[17] among which iron nitrides such as a mixed Fe_3N/Fe_4N catalyst, grown on a graphene/Ni foam support,[18] Fe_3N NPs on carbon nanotubes (CNTs),[19] and Fe_2N embedded in mesoporous TiO_xN_y nanoshells.[8]

In parallel to the search for water electrolysis catalysts, efforts are also being deployed to search for efficient catalysts for the CO_2 reduction reactions (CO_2RR). Indeed, reducing the CO_2 – being a greenhouse gas – into chemicals with added value

[a]*Université de Toulouse, CNRS, LCC, 205 route de Narbonne, BP 44099, F-31077 Toulouse Cedex 4, France. E-mail: catherine.amiens@lcc-toulouse.fr*
[b]*Université de Toulouse, CNRS, CEMES, 29 rue Jeanne Marvig, F-31055 Toulouse, France*
[c]*Laboratoire de Génie Chimique, Université de Toulouse, CNRS, INPT, UPS, 118, route de Narbonne, Toulouse, 31062, France*
[d]*Centre Inter-universitaire de Recherche et d'Ingénierie des Matériaux, INP-ENSIACET, CNRS, Université de Toulouse, 118, route de Narbonne, 31062 Toulouse, France*
[e]*University of Science and Technology of Hanoi, Vietnam Academy of Science and Technology, 18 Hoang Quoc Viet, Nghia Do, Hanoi, Vietnam. E-mail: tran-dinh.phong@usth.edu.vn*
[f]*NanoMePS, Département Génie Physique INSA, 135 avenue de Rangueil, 31 077 Toulouse Cedex 4, France*

such as CO, HCOOH, CH_3COOH, *etc.* would be an ideal strategy to tackle the CO_2 gas emission challenge. Copper-based nanomaterials are the most exploited CO_2RR catalysts which showed a large variety of product selectivity ranging from C1 to C2+ compounds.[20] Recently, by combining the high-throughput DFT and machine learning screening, Yohannes *et al.* have reported the nitrides of Co, Cr, and Ti as potential catalysts for the CO_2RR, theoretically.[21] However, to the best of our knowledge, there is still a lack of experimental demonstration on the use of transition metal nitrides as electrocatalyst for the CO_2RR.

Regarding the material synthesis, transition metal nitrides usually require multistep synthetic processes and drastic conditions (in terms of temperature) which limits their usage. For example, ε-Fe_2N NPs have been prepared from the pyrolysis of iron salts in the presence of ammonia ($T > 700$ °C),[8–12,22] or by direct nitridation of Fe oxide[23–27] or oxyhydroxide NPs[28–30] ($T >$ 500 °C). All these drastic conditions have the drawback of hindering the control over the morphology of the final nanomaterial due to roughening and sintering.[31] Alternatively, ε-Fe_2N NPs were successfully synthesized from Fe oxide NPs in a two-step process involving first their reduction under hydrogen into Fe NPs, then nitridation thereof with a H_2/NH_3 gas mixture. This approach allowed to reduce the nitridation temperature close to 400 °C.[32] However, intermediate ill-defined Fe nanomaterials, where the morphology and size distribution of the primary Fe oxide NPs is lost, may be observed. The reactivity towards ammonia depending on the specific surface area of each NP, a mixture of phases is observed when the morphology distribution is too large.[33] High temperature processes may also favor the formation of the more stable ζ-Fe_2N phase which is less interesting for the catalysis.[27,34] Synthesis procedures allowing less drastic conditions are thus on demand. The first attempt at the development of a low temperature process involved solvothermal synthesis using iron azide as a precursor.[35] ε-Fe_2N NPs of circa 26 nm large could be obtained after 7 days at 270 °C. However, it rises safety concerns given the high thermal instability and shock sensitivity of such a precursor. Therefore, we hypothesized that starting directly from small, morphology controlled, zerovalent Fe NPs (ZVFeNPs) could be a good strategy to reach small, morphology and composition controlled iron nitride NPs as the NH_3 dissociation, being the limiting step of the nitridation process, is easier on Fe than on its oxides.[36] It would thus allow to decrease the reaction temperature, and get iron nitride nanomaterials with well-controlled composition, structure and morphology, reflecting the initial morphology of the ZVFeNPs, as sintering and coalescence would be avoided. The small size of the final iron nitride NPs would be an added advantage for catalytic applications, given their high surface specific area.

For this purpose, we took benefit from the organometallic approach to zerovalent metal NPs. Indeed, ZVFeNPs of well-controlled size (spanning the 1.5–15 nm range) and well-controlled morphology can be efficiently synthesized by hydrogenation of the commercially available bis-trimethylsilylamido Fe(II) complex, $[Fe(N(SiMe_3)_2)_2]_2$, in the presence of stabilizing ligands such as amines or/and carboxylic acids, and are even commercially available in some cases.[37–40] These NPs show a high surface reactivity at moderate temperature, namely ≤200 °C. For instance, it was shown that in presence of hydrogen they display surface hydrides and can catalyze the hydrogenation of unsaturated C–C bonds.[41] The study of their reactivity with carbon monoxide evidenced a CO dissociation at their surface in mild conditions, a property that has been exploited to form air stable Fe carbide NPs which retained the morphology of the native ZVFeNPs.[42] On the basis of these previous results, we considered that such NPs might be good candidates for investigating the dissociation of NH_3 with the aim to incorporate N atoms in the bcc-Fe structure, and if possible in a controlled way, in order to get iron nitride nanomaterials as defined as possible.

To examine our hypothesis, in this work we applied mild reaction conditions in terms of temperature and pressure for preserving the initial morphology of the ZVFeNPs. The ZVFeNPs used in this work consist of single-crystalline NPs of circa 10 nm in size. By this method, we were able to synthesize ε-Fe_2N nanomaterial in the pure phase and in a reproducible manner. Furthermore, we demonstrate that this method is applicable to the preparation of thin layers of ε-Fe_2N NPs on electrodes and report on preliminary assessment of their electrocatalytic activities for the OER and CO_2RR.

2. Results and discussion

2.1. Nanostructured ε-Fe_2N powders

The ZVFeNPs used in this study were prepared by the hydrogenation of $[Fe(N(NSiMe_3)_2)_2]_2$ complex in the presence of a mixture of palmitic acid (1.2 equiv.) and hexadecylamine (1 equiv.) in mesitylene at 150 °C (Scheme 1). After 48 h, the reacting medium was cooled down to room temperature and the NPs formed were precipitated by addition of acetone and isolated with a magnet. The isothermal magnetization curve recorded at 2.5 K (after a field cooling procedure from r.t. under 5T) was found to be symmetrical, displaying a hysteresis with a low coercive field of 90 mT, and a magnetization of 200 A m^2 kg_{Fe}^{-1} at 5T that was in agreement with the formation of ZVFeNPs (Fig. SI1) and excluded surface oxide contamination. The TEM images (Fig. SI2) show NPs that are mainly spherical with a minor content of cube-like ones, with an average size of 10.1 ± 1.4 nm. XRD measurements (Fig. SI3) evidenced only the bcc-Fe phase, with a crystallite size of 9.3 nm as determined from the Scherrer equation. The good agreement between the size determined from TEM and XRD measurements points out the single crystalline character of these NPs.

Given their reduced size, well-controlled morphology and absence of surface oxidation, these ZVFeNPs appeared to be a suitable starting nanomaterial to develop the synthesis of Fe nitrides by direct reaction with NH_3. The challenge was to achieve the diffusion of nitrogen in the iron structure while maintaining the initial morphology of the NPs during the process.

In order to avoid coalescence during the nitridation process, the ZVFeNPs should present a good enough surface reactivity enabling to work at as low temperatures as possible. The absence of any surface oxide layer on the Fe NPs was already

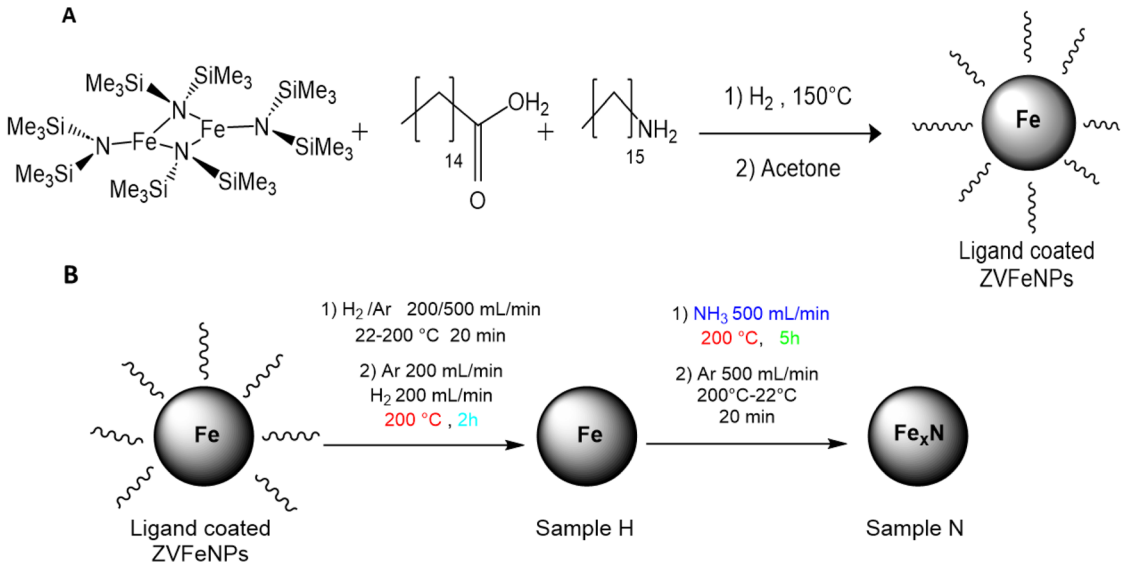

Scheme 1 (A) Synthetic approach to ZVFeNPs; (B) activation and nitridation conditions leading to H and N samples, respectively.

favorable. However, to further enhance the surface reactivity of the NPs, a mild thermal treatment was performed in order to remove the surface ligands and thus provide more accessible iron sites. In addition, this treatment was conducted in the presence of H_2 in order to prevent any adventitious oxidation, as the NPs would be particularly reactive once the ligands removed. Typically, after introduction under inert atmosphere in a tubular furnace, the ZVFeNPs were exposed to a H_2/Ar flow (v/v 1/1, with a flow rate of 200 mL min^{-1} each) at 200 °C for 1 h (Scheme 1). During this step, a slight volume loss was the only change observed, which could account for the densification of the powder following the removal of ligands. Indeed, ICP analysis revealed the Fe content varied from 75 w% before the thermal treatment (namely in the ZVFeNPs sample) to 99.6 w% after the thermal treatment (hereafter referred as **Sample H** where H stands for after Hydrogen treatment). Magnetic measurements (Fig. SI4) confirmed the absence of oxidation after thermal treatment. As well XRD analysis confirmed that the bcc structure and crystallite size of the nanomaterial were preserved (crystallite size 9.2 nm in **Sample H**) (Fig. SI5).

For the nitridation step, the H_2/Ar flow was replaced by an NH_3 flow (500 mL min^{-1}) while keeping the temperature at 200 °C (Scheme 1). After 5 h, the powder was allowed to cool down to room temperature under an Ar flow (500 mL min^{-1}). The sample was referred as **Sample N** where N stands for after nitridation.

The powder recovered could not be dispersed in any organic solvent. The morphology and local structure of the nanomaterial were first studied by SEM (scanning electronic microscopy). Despite the inherent difficulty in imaging so small nanostructures, SEM images showed that the powder consisted of grains with sizes in the nanoscale range (Fig. 1a). However,

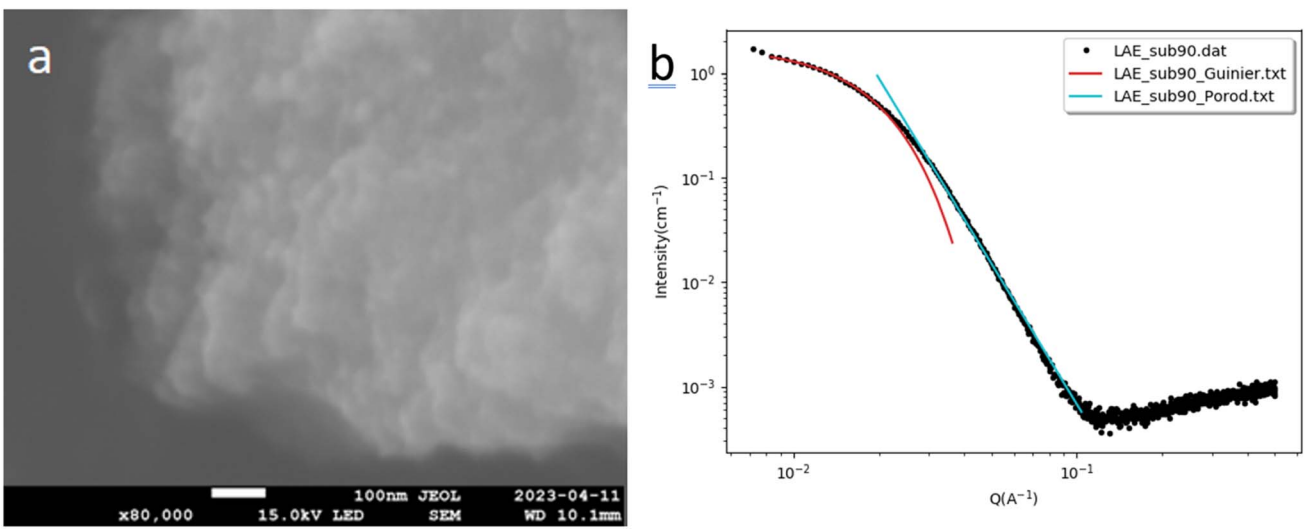

Fig. 1 (a) Typical SEM image of the nitridated material (scale bar: 100 nm); (b) SAXS data and corresponding fit.

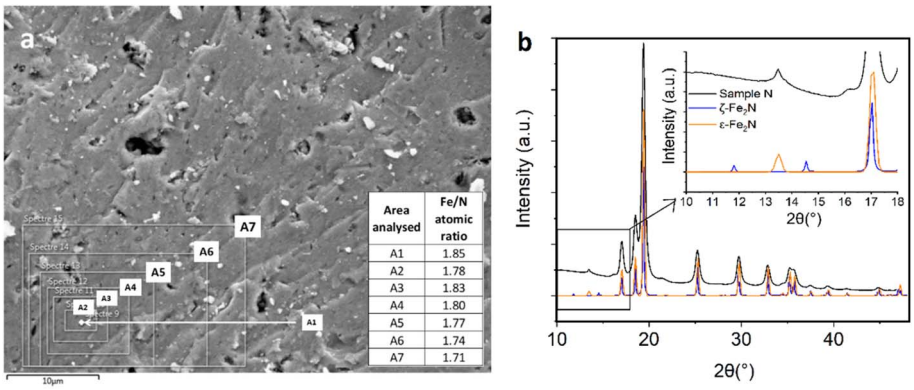

Fig. 2 (a) SEM image of the nitridated material and Fe/N atomic ratios derived from EDX analysis on the various surface areas showcased; (b) XRD diagram of the nitridated material (black line) in comparison to ε-Fe_2N (orange line, ICSD33575) and ζ-Fe_2N (blue line, ICSD152811) reference diagrams with inset showing an enlargement of the diagrams in the low angles window.

the resolution and statistics are too poor to conclude on the exact morphology of these grains.

SAXS analysis was then performed to get more precise, as well as statistical, information. Fig. 1b shows the SAXS curve obtained for **Sample N**. Its shape does not correspond to any known simple form factors, such as spheres or cubes, likely due to the heterogeneity of the sample. However, the application of a simple, shape-independent model like the "Guinier-Porod" model, available in SASVIEW[43,44] allowed us to determine an average gyration radius (R_g) of 9.1 nm and the Porod decay (4.0). So, no extended coalescence was detected.

A combination of chemical and elemental analysis evidenced Fe and N contents of 89.3 w%, and 10.2 w%, respectively which pointed out a composition close to Fe_2N (actually, $Fe_{2.2}N$). EDX analysis performed on different surface areas also indicated a Fe/N ratio close to 2, although, due to the possible surface adsorption of ammonia or ammonia derived N containing species, the results afforded by this surface analysis technique should be taken with care. Nonetheless, these results evidenced the compositional homogeneity of the material (Fig. 2). Raman spectroscopy was also in agreement with the formation of a Fe_2N nanomaterial, as vibrations at 210, 272, 381 and 586 cm^{-1} were observed in agreement with previous results from the literature[24,45] (Fig. SI6). The high reactivity of the organometallic ZVFeNPs towards ammonia is thus confirmed, as a homogeneous material (in terms of composition) with high nitrogen content could be obtained.

Close to the Fe_2N composition, ε and ζ phases exist in the iron nitride phase diagram.[46] The powder XRD diagram of **Sample N** (Fig. 2b) displayed well-defined diffraction peaks. At low angles, both the absence of peaks at 11.8° and 14.5°, and the presence of the peak at 13.5° indicate that only the ε phase was formed, thus highlighting the homogeneity of the material, and a perfect control over its structure. The Rietveld analysis further confirmed the formation of the ε phase (trigonal unit cell, space group: *P*312) (Fig. SI7). During Rietveld refinement, once the Full Profile Matching was complete, when the thermal motions of the four atoms of the unit cell were released, the thermal motion of the N3 atom was stronger than the one of the others (Fig. SI7, bottom). This is indicative of N vacancies on the N3 site. This behavior was observed in all refinements performed on a series of nitridated samples. Given the limitations of our experimental set-up (refer to Experimental section for details), the occupancy rate could not be deduced with enough accuracy from the Rietveld refinement. Rather, this occupancy rate was obtained from the cell parameters and the Vegard law.[47,48] Indeed, for the determination of the cell parameters, only the positions of the peaks are taken into account, and the obtained parameters presented good uncertainty values (esd). From these data, a composition fluctuating from $Fe_{2.06}N$ to $Fe_{2.04}N$ could be deduced. The size of the crystallites was evaluated using the Scherrer equation, showing a value of close to 15 nm. This value is in good agreement with the size of the grains determined by SAXS (18.2 nm). It is larger than the crystallite size of the primary ZVFeNPs (10 nm). This size expansion is too large to be solely attributed to the insertion of N in the NPs, and suggests that some atomic redistribution occurs upon nitridation of the ZVFeNPs. Still, these results clearly confirm the high surface reactivity of the ZVFeNPs towards the dissociation of ammonia

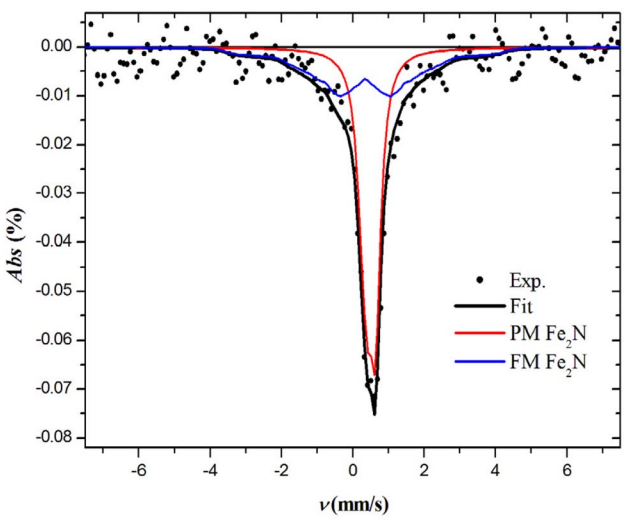

Fig. 3 Mössbauer spectrum of the nitridated material recorded at 80 K (dots) and best fit obtained (black line) from a combination of a paramagnetic Fe_2N contribution (PM Fe_2N, red line), and a ferromagnetic Fe_2N contribution (FM Fe_2N, blue line).

N–H bonds, as a high N content phase was formed in milder conditions than the mildest previously reported.[35,36] It further indicates that the nitridation conditions were mild enough to prevent extended coalescence of the ZVFeNPs but high enough to ensure homogeneous diffusion of N inside the ZVFeNPs, thus affording a nanomaterial that consists in crystalline ε-Fe_2N grains. To the best of our knowledge, it also affords the smallest ε-Fe_2N grains reported so far.

The Mössbauer spectrum of **Sample N** has been recorded at 80 K with a ^{57}Co source in a Rh matrix and calibrated against the bulk bcc-Fe (Fig. 3, dots). The best fit of the experimental data has been achieved by taking into account a set of contributions of ε-$Fe_{2+x}N$'s characteristics, where $x \leq 0.2$.[49,50] Interestingly, we do not observe any broad hyperfine Fe oxide contribution, which confirms the absence of crystalline iron oxide. We introduced the contributions of two kind of paramagnetic species with isomer shifts of 0.52 and 0.45 mm s^{-1} and quadrupolar splitting 0.23 and 0.42 respectively (see Table SI1). These two contributions are combined as PM Fe_2N in Fig. 3 (red line) to ease its reading. Note the presence of a contribution related to ferromagnetic like nanomaterial (FM Fe_2N, blue line, Fig. 3), with a broad hyperfine field distribution range from 3 to 32T (Fig. SI8). Since the Curie temperature for ε-$Fe_{2+x}N$ material with $x \leq 0.2$ is less or close to 80 K,[51] such a paramagnetic like behavior and broadened distribution of hyperfine field for the ferromagnetic contribution are expected. Indeed, such a broadening of the perfect sextet lines related to FM order is a consequence of the superparamagnetic relaxation in NPs.

The hysteresis cycles measured at 5 K and 300 K (Fig. SI9), evidenced a low magnetization value of 48 A m^2 kg^{-1} of iron at 5T, (not saturated), and paramagnetic like behavior at room temperature with a magnetization value of 12 A m^2 kg^{-1} of iron at 5T. Such a behavior is qualitatively consistent for a ε-$Fe_{2+x}N$ nanomaterial where $x \leq 0.2$, since, the ferromagnetic behavior vanishes as the nitrogen content reaches the ratio of 2 N atoms per 1 Fe atom.[51] Moreover, as the hysteresis cycle at 5 K was done after a field cooling procedure, its symmetry rules out the presence of exchange bias, thus excluding the presence of ferrimagnetic or antiferromagnetic phases.

The nitridation process was repeated many times and gave consistent results. Each time clearly and consistently evidenced the formation of nanostructured ε-Fe_2N as exemplified in Fig. SI10 (XRD), Fig. SI11 (EDX), and in Table SI2 which reports the phase identified, crystallite sizes, composition and magnetization for three typical batches of nitridated powders (samples N1, N2 and N3). As shown in Fig. SI12 the gyration radii determined by SAXS varied between 7.9 (Porod value: 4.0) and 9.1 nm (Porod value: 4.0).

2.2. Nanostructured ε-Fe_2N deposits on electrodes

Building on the results described above, and motivated by possible applications of this nanomaterial in electrocatalysis, we undertook the preparation of modified FTO or glassy carbon electrodes on which the ε-Fe_2N NPs would be deposited. As aforementioned, the as-prepared ε-Fe_2N powders are difficult to redisperse in liquid media. Thus, we attempted to produce the ε-Fe_2N nanostructured deposits by direct nitridation of ZVFeNPs deposited on FTO substrates. To do so, a suspension of the ZVFeNPs in toluene was prepared. A low quantity of oleic acid was added to the suspension to improve the dispersion of the NPs. A few drops of this suspension were deposited on the FTO substrates maintained at 50–60 °C to facilitate the solvent evaporation, and improve the homogeneity of the deposit (Fig. 4a). The quantity of ZVFeNPs could be easily adjusted by adjusting the volume of the suspension that was drop-casted on the substrates (see Experimental section). Then the films obtained were nitridated following the procedure described above. No change could be observed by naked eyes after the nitridation step (Fig. 4b). The SEM imaging indicated that the nanostructure was preserved (see below, Electrocatalysis section). Raman spectra show characteristic vibration bands of Fe_2N at 211, 274, 383 cm^{-1} (Fig. SI13), thus confirming the formation of Fe_2N on the FTO substrate.[45] Scratching the nitridated layer from the FTO surface allowed to collect enough powder for XRD analysis that clearly evidenced the formation of the ε-Fe_2N phase (Fig. SI14). A crystallite size of 10.4 nm was determined according to the Scherrer equation. Moreover, a suspension of this material in ethanol could be prepared and drop-casted on TEM grids. Although it is not fully representative as the material is difficult to disperse, the TEM images show NPs with a size close to 10 nm (Fig. 4c) which confirms the nanostructure of the deposit. Putting together the available data, the successful formation of a nanostructured ε-Fe_2N layer on the FTO substrate was confirmed (code name **Fe_2N/FTO**).

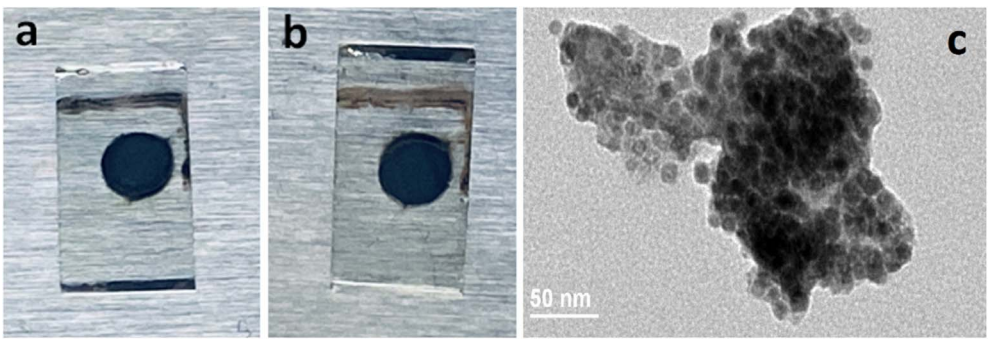

Fig. 4 Photographs of a typical modified FTO electrode before (a) and after (b) nitridation and (c) TEM image of the nitridated deposit after scratching from the electrode, being suspended in toluene and drop-casted on a carbon-coated copper grid (scale bar 50 nm).

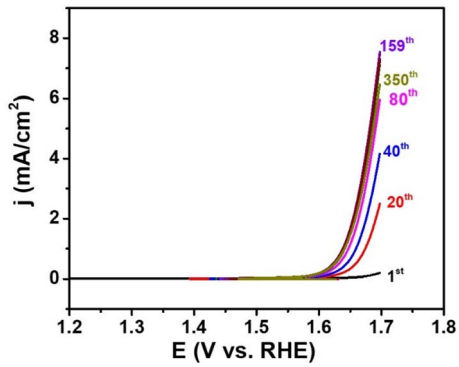

Fig. 5 *I–V* curves recorded for a Fe_2N/FTO catalyst electrode immersed in a 1.0 M KOH electrolyte solution. Linear sweep voltammograms were recorded with a slow potential scan rate of 5 mV s^{-1}.

To avoid possible carbide formation, graphite electrodes were simply modified by drop casting of a suspension of the preformed ε-Fe_2N powder, although it led to deposits of lesser homogeneity.

2.3. Electrocatalytic activity of ε-Fe_2N NPs

2.3.1. For the oxygen evolution reaction (OER). The nanostructured ε-Fe_2N material was first examined as an electrocatalyst for the oxygen evolution reaction, in an alkaline electrolyte, namely a 1.0 M KOH (pH = 13.5) solution. To this end, the ε-Fe_2N nanomaterial grown on FTO substrate (sample **Fe_2N/FTO**) was used as catalyst electrode. Fig. 5 shows subsequent *I–V* curves recorded by linear sweep voltammetry with a relative slow potential scan rate of 5 mV s^{-1}. It can be seen that the catalytic current density increased when repeating the potential polarization and reached the highest values after 159th potential polarization scans. It suggests a slow catalyst activation process. Hereafter, the catalyst obtained after 159th potential polarization scans will be referred to as the activated Fe_2N/FTO catalyst. We note that, further repeating the potential polarization scan on the activated Fe_2N/FTO catalyst electrode induced a gradual decrement of the catalytic current density caused by a physical detachment of the ε-Fe_2N NPs from the FTO electrode surface. Indeed, ICP-MS analysis showed the presence of iron in the electrolyte solution after performing the 350th potential polarization. On the basis of the iron amount quantified, the loss of initial mass of ε-Fe_2N NPs during the catalysis was deduced to be ~9%.

Fig. 6 shows the 159th *I–V* curve recorded for the activated Fe_2N/FTO catalyst electrode immersed in a 1 M KOH electrolyte solution, namely the one showing the highest catalytic current, together with the corresponding Tafel plot. Actually, the blank FTO electrode without any catalyst decoration showed a negligible anodic current in the potential window examined. Hence, the catalytic current recorded for the activated Fe_2N/FTO catalyst electrode was purely originated from the OER catalyzed by the ε-Fe_2N catalyst. It can be seen that, the catalytic current emerged at an onset potential of 1.55 V *vs.* RHE corresponding to an overpotential requirement of 320 mV. The Tafel slope was calculated to be 57.8 mV per decade, indicating a fast OER kinetics. However, these performances are lower than those previously reported for the Fe_3N/graphitic carbon requiring an overpotential of 281 mV,[52] Fe_2N/TiO_xN_y requiring an overpotential of 316 mV,[8] Fe_3N–Fe_4N/Ni-foam requiring an overpotential of 238 mV,[53] or the Fe_3N/CNTs requiring an overpotential of 218 mV.[54] We note that the FTO electrode support used in this work is a flat electrode which has a significantly lower surface area in comparison to 3D Ni-foam, graphitic carbon or CNTs electrode supports used in the previous studies. Therefore, the aforementioned comparison of catalytic performance should be taken with care.

In order to gain more insights into the catalyst activation, we first examined the surface wettability of the Fe_2N/FTO catalyst electrode. Herein, the surface wettability was evaluated *via* the static water contact angle measurement at three different states, namely the as-prepared Fe_2N/FTO electrode, the activated Fe_2N/FTO electrode showing the highest catalytic current density (thus, after 159 potential polarization scans), and the same electrode after 350 potential polarization scans accompanied with a partial detachment of ε-Fe_2N catalyst. As shown in

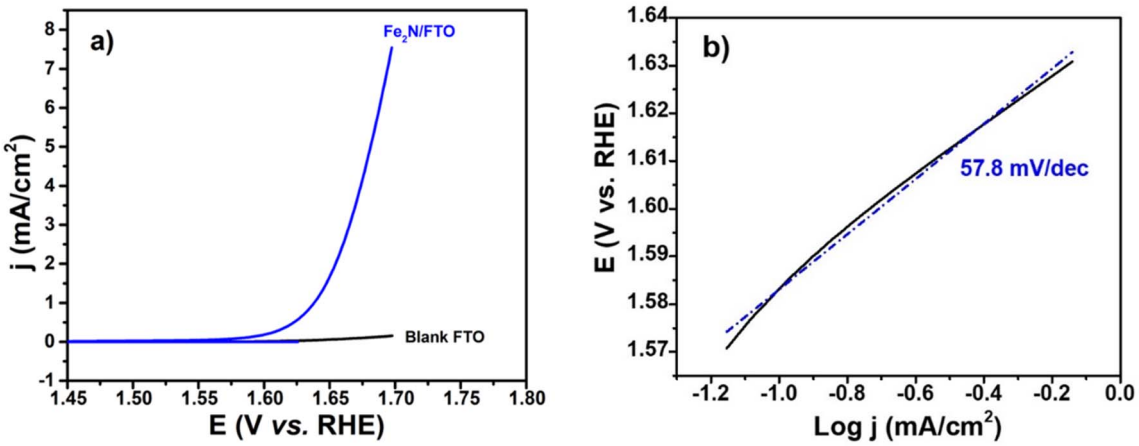

Fig. 6 (a) The 159th *I–V* curve recorded for the Fe_2N/FTO electrode (blue line) and the steady *I–V* curve recorded for the blank FTO electrode (black line) immersed in 1.0 M KOH solution with a slow potential rate of 5 mV s^{-1} (b) Tafel plot from the *I–V* curve of Fe_2N/FTO electrode for the slow reaction rate region.

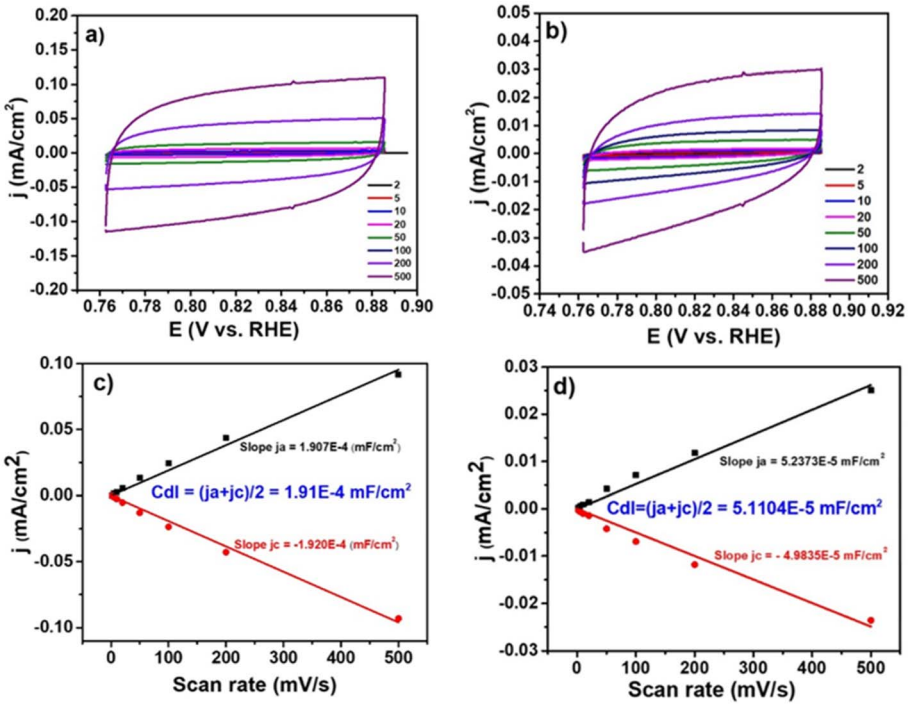

Fig. 7 Cyclic voltammograms recorded at different potential scan rates for: (a) an as-prepared Fe_2N/FTO catalyst electrode and (b) an activated Fe_2N/FTO catalyst electrode. Plotting of the current density obtained at 0.82 V *vs.* RHE in function of potential scan rates for the case of: (c) as-prepared Fe_2N/FTO catalyst electrode and (d) activated Fe_2N/FTO catalyst electrode. Electrolyte was a 1.0 M KOH solution.

Fig. SI15, the as-prepared Fe_2N/FTO electrode exhibits a moderate water contact angle of 90.5°, indicating a moderate hydrophilic character of the catalyst's surface. When the Fe_2N/FTO electrode was activated to reach the highest catalytic current density, the water contact angle was reduced from 90.5° to 75.2° (Fig. SI15b). It implies that the wettability of catalyst's surface increased during the catalyst activation process. Such wettability (hydrophilicity) is favorable for a rapid evolution of O_2 gas bubbles from the catalyst's surface and increasing the accessibility of the electrolyte to the catalytic active surface. Both these two favorable features resulted in a significant enhancement of catalytic activity of the Fe_2N/FTO catalyst electrode. Expanding the potential polarization on the activated Fe_2N/FTO catalyst electrode caused a partial detachment of ε-Fe_2N but didn't cause any significant change in its surface wettability (Fig. SI15c).

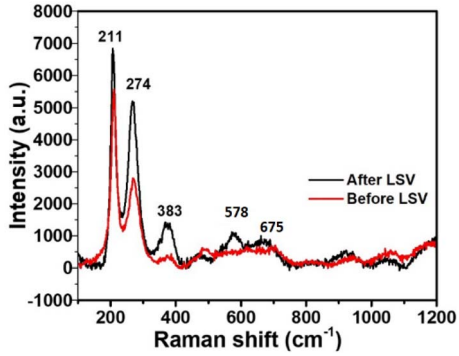

Fig. 8 Raman spectra recorded for an as-prepared Fe_2N/FTO catalyst electrode (red trace) and an activated Fe_2N/FTO catalyst electrode (black trace). Excitation was made by a 532 nm laser.

The electrochemical surface area (ECSA) of the Fe_2N/FTO catalyst electrode was evaluated by measuring its electrochemically effective double-layered capacitance (C_{dl}) (Fig. 7). The C_{dl} was determined to be 1.91×10^{-4} mF cm^{-2} for the as-prepared Fe_2N/FTO catalyst electrode and 5.1×10^{-5} mF cm^{-2} for the activated Fe_2N/FTO catalyst electrode. The decrement of C_{dl} by ~3.7 times clearly indicates a decrement of the electrochemical surface area that can be attributed to the partial detachment of ε-Fe_2N from the FTO substrate during the activation process.

SEM analysis was performed to visualize the morphology of the Fe_2N/FTO catalyst electrodes. The as-prepared Fe_2N/FTO catalyst and the activated Fe_2N/FTO catalyst showed similar morphology (Fig. SI16). It means that the catalyst activation caused insignificant change in the size and shape of the Fe_2N grains. Few cracks can be observed across the activated Fe_2N/FTO electrode surface (Fig. SI16d) which can also contribute to the decrement of its electrochemical surface area in comparison with the as-prepared one.

Raman spectroscopic analysis was performed in order to track the chemical changes that potentially occurred during the catalyst activation. Fig. 8 shows the spectra recorded for the as-prepared Fe_2N/FTO catalyst electrode (red curve) and the activated Fe_2N/FTO catalyst electrode (black curve). It can be seen that the characteristic vibration bands of the Fe_2N material at 211, 274 and 383 cm^{-1} were still observable in the activated Fe_2N/FTO catalyst. The broad vibration bands that emerged at *ca* 578 and 675 cm^{-1} may be assigned to goethite α-FeOOH.[55,56] A comparable behavior was reported by Wang *et al.* when

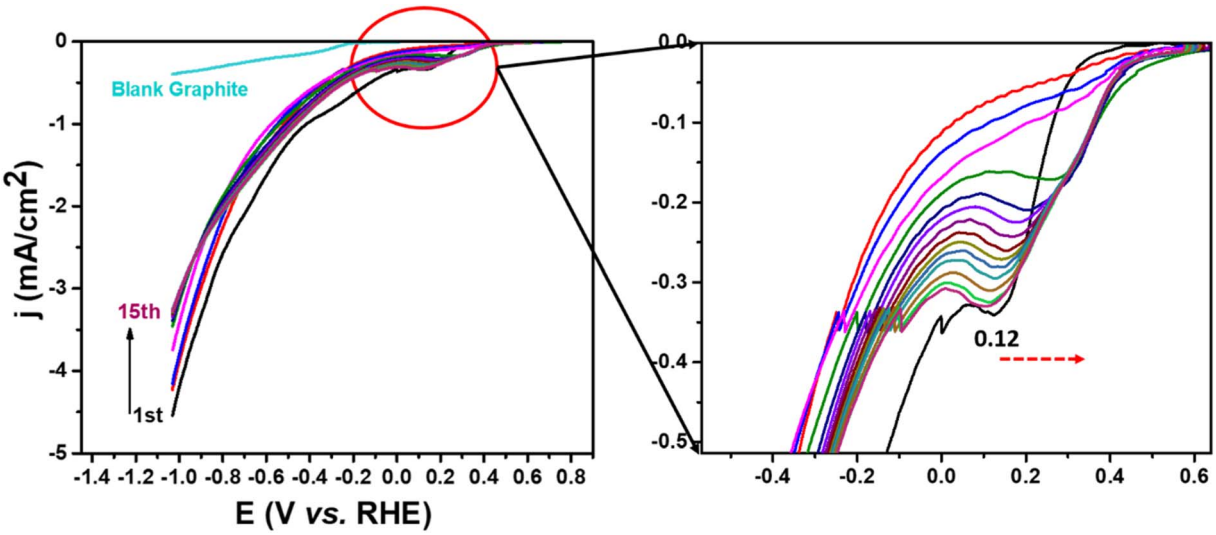

Fig. 9 Subsequent *I*–*V* curves recorded on a ε-Fe_2N/graphite catalyst electrode immersed in a 0.1 M $NaHCO_3$ (pH 6.8 solution) saturated CO_2 gas. Potential scan rate was 5 mV s^{-1}.

studying the electrocatalytic activity of Fe_3N NPs deposited on CNTs in OER.[19] The results imply an electrochemical oxidation of the surface iron nitride generating a layer of iron oxide, thus generating a type of Fe_2N@FeO_x core@shell structure. In other words, the iron nitride to iron oxide electrochemical oxidation was the origin of the catalyst activation observed. We note that such a phenomenon has been reported for other metal nitrides, *e.g.* the Fe_3N/Fe_4N and the Co_4N catalyst in OER.[57,58]

2.3.2. For the CO_2 reduction reactions (CO_2RR). In this work, we examined for the first time the ability of a nanostructured ε-Fe_2N material for catalyzing the CO_2RR. To this end, FTO electrode was not appropriate because it suffered of the reductive corrosion at high reducing potential. Therefore, we employed a graphite electrode as the electrode support on which ε-Fe_2N (from **Sample N**) was drop-casted. The resultant ε-Fe_2N/graphite catalyst electrode was assayed in a 0.1 M $NaHCO_3$ electrolyte solution saturated with CO_2 (pH 6.8). The first potential polarization exhibited a reduction event at 0.12 V *vs.* RHE prior to the emerging of the cathodic current (Fig. 9). This reduction event experienced an anodic shift when repeating the potential polarization scans. We attribute this reduction event to the Fe_2N/Fe redox couple[59] on the surface of Fe_2N NPs which can be shifted to less reductive potential (anodic shift) when the Fe_2N NPs get more disordered because of the potential polarization.

In order to examine the product selectivity of the CO_2RR on the ε-Fe_2N/graphite catalyst electrode, the bulk electrolysis was conducted for 1.5 hours at −0.7, −0.8, −0.9, and −1.0 V *vs.* RHE. Rather stable catalytic current densities were achieved at these potentials (Fig. 10) suggesting a good stability of the ε-Fe_2N catalyst under these operating conditions. Gas chromatography was conducted to analyze the gaseous products. Only H_2 was found but no other gas like CO, methane, ethane. At all reduction potential assayed, H_2 was the dominant product with an average Faradaic Efficiency (FE) of 74–82% (Fig. 11, yellow column). Ionic chromatography was used for analyzing the products in solution, revealing the production of formate ($HCOO^-$) and acetate (CH_3COO^-) at all reduction potentials assayed. Actually, acetate was produced with considerable efficiencies at all potentials applied. At −0.9 V *vs.* RHE, the highest FE of ~6.2% for acetate formation was achieved. These results show that on the current ε-Fe_2N catalyst the HER is significantly favorable *versus* the CO_2RR. Even though, this represents the first report of the CO_2-to-CH_3COO^- electrochemical reduction for a metal nitride catalyst.

As the nanostructured ε-Fe_2N catalyst experienced an oxidative activation generating iron oxide species during the OER (see this above), we were interested to investigate how this catalyst behaved during the catalytic CO_2RR process. Fig. 12 shows SEM images collected on the ε-Fe_2N/graphite electrode after being conditioned at −0.7 V *vs.* RHE in the 0.1 M $NaHCO_3$ solution saturated with CO_2 gas for 1.5 hours. Formation of crystals of nanoflake morphology is clearly observed. The morphology change was also obvious when conditioning the ε-Fe_2N/graphite electrode at other potentials (Fig. SI17). The EDX elemental mapping showed the presence of Fe, O, C and N elements in the nanoflakes (Fig. 13). The atomic percentage of Fe and O elements was deduced to be 20

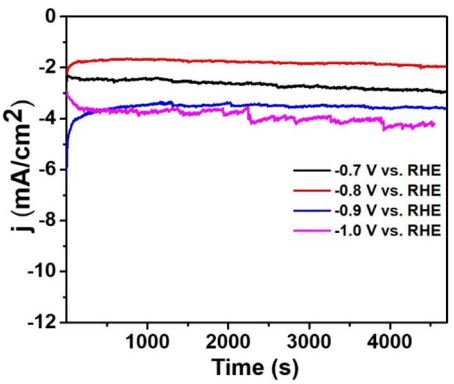

Fig. 10 *I*–*t* curves recorded during the bulk electrolysis at −0.7 V, −0.8 V, −0.9 V and −1.0 V *vs.* RHE employing a ε-Fe_2N/graphite catalyst electrode. Electrolyte was a 0.1 M $NaHCO_3$ solution saturated with CO_2.

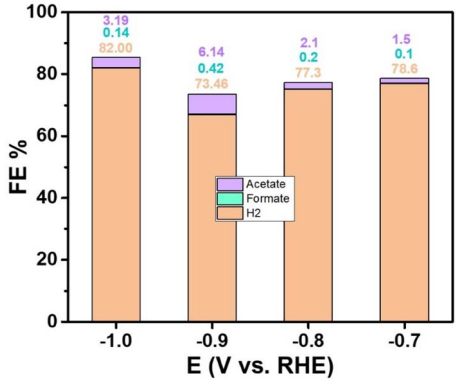

Fig. 11 Product selectivity obtained at different potentials employing a ε-Fe_2N/graphite catalyst electrode. Electrolyte was a 0.1 M $NaHCO_3$ solution saturated with CO_2 gas.

and 71%, respectively. It suggests the formation of iron oxide species FeO_x on the surface of ε-Fe_2N/graphite electrode.

Raman spectroscopic analysis showed the remaining of vibration bands at 211 to 383 cm^{-1} which are characteristic for the Fe_2N material (Fig. 14 and SI18). A new strong broad peak emerged in the 650–750 cm^{-1} window which is assignable to the A1g vibration mode of Fe–O, in many iron oxide phases such as magnetite, or maghemite, or even to goethite.[60] The Raman results are in good agreement with SEM and EDX data and support the formation of magnetite which has the nanoflakes morphology.

X-ray photoelectron spectroscopy (XPS) analysis of a spent catalyst is displayed in Fig. SI19. The Fe2p signal can be attributed to Fe(III) species (binding energy around 711.3 eV), suggesting that the surface of the magnetite crystals is oxi/hydroxydized. A satisfactory fit of the $Fe2p_{3/2}$ region could be obtained by taking into account FeOOH contributions, although minor traces of Fe_2O_3 cannot be excluded.[61]

3. Experimental

3.1. Materials and techniques

All the gases used—H_2 (99.999%, <3 ppm H_2O, <2 ppm O_2, <1 ppm CO, <1 ppm CO_2), NH_3 (99.999%, <3 ppm H_2O, <2 ppm O_2), and Ar (99.999%, <3 ppm H_2O, <2 ppm O_2)—were supplied by Air Liquide. Glove-box (MBraun, <1 ppm H_2O, <1 mmol O_2) and Ar-vacuum line were used for the preparation of the samples. Ar used in the vacuum line was purified through a 4 Å activated molecular sieve and a copper catalyst. Toluene (99%, VWR) was purified using a Braun purification system (SPS-800), then degassed by the freeze–pump–thaw method. A water content below 5 ppm was controlled by the Karl Fischer method with a Metrohm KF Coulometer. Hydrochloric acid (Sigma Aldrich), nitric acid (Carlo Erba, 69.5%), oleic acid (Alpha Aesar, 99%), $NaHCO_3$ (Sigma Aldrich, ACS reagent, ≥99.7%), 2-propanol (IPA, Sigma Aldrich, 99.9%), Nafion (Sigma Aldrich, 5 wt% in mixture of low aliphatic of alcohols and water) were used as received. FTO slides were cleaned by sonication for 30 minutes first in acetone (Sigma-Aldrich, ≥99.5%) and 30 minutes in EtOH (Sigma-Aldrich, anhydrous, >99.9%) and then dried at ambient temperature for 1 h before use.

Transmission Electron Microscopy (TEM) images were collected on a JEOL 1011 microscope at UAR Raimond Castaing. Sample preparation involved depositing a few drops of the colloidal solution in toluene onto a carbon-coated copper grid. Samples were dried under vacuum using a secondary vacuum pump for a minimum of 2 hours. Size distributions were obtained from the microscopy images using the open-source software ImageJ, with a minimum of 200 NPs measured to ensure statistical significance. The size distributions were modeled as Gaussian distributions using Origin software, with results expressed as mean ± standard deviation. *Scanning Electron Microscopy (SEM) images* were collected at the Raimond Castaing Center with a JEOL 7800F microscope equipped with a Field Emission Gun (FEG). The samples were placed on carbon tape, adhered to an aluminum stub, and then dried under secondary vacuum (10^{-5} mbar) overnight before observation. *Energy Dispersive X-ray analysis* (EDX) were conducted on the JSM-7800F Prime at the Raimond Castaing Center. Samples were prepared in two forms: as a powder placed on carbon tape and as a thin layer of iron nitride solute in toluene applied to FTO electrodes. *Powder X-ray data* were collected in transmission mode at room temperature on a PANalytical X'Pert PRO MPD powder diffractometer with Bragg–Brentano theta/theta geometry (step size [°2θ] = 0.0170), equipped with a standard Mo X-ray tube ($\lambda_{K\alpha1}$ = 0.709319 Å and $\lambda_{K\alpha2}$ = 0.713609 Å), a linear X-Celerator detector, a capillary sample holder and a focusing mirror after the tube or on a homemade diffractometer based on a Rigaku® MM007HF generator equipped with a Mo rotating anode ($\lambda_{K\alpha1}$ = 0.709319 Å and $\lambda_{K\alpha2}$ = 0.713609 Å) at 50 keV and 24 mA, combined with Osmic focusing multilayers optics, a RAXIS4++ image plate detector

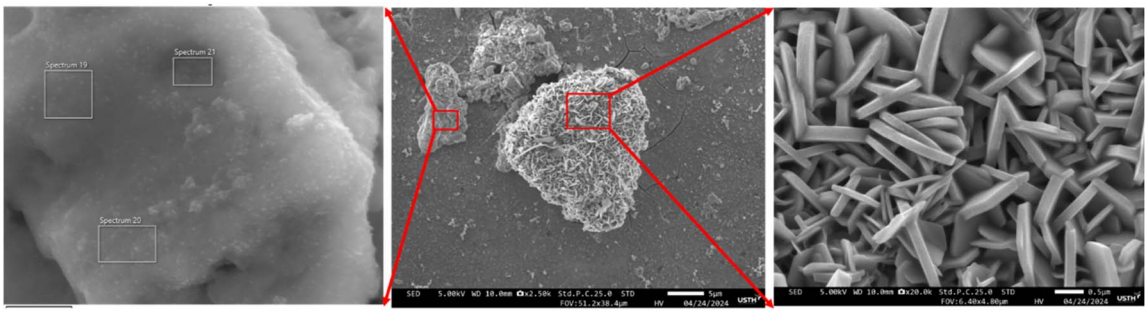

Fig. 12 SEM images taken on a ε-Fe_2N/graphite catalyst electrode after being conditioned at −0.7 V *vs.* RHE in a 0.1 M $NaHCO_3$ solution saturated with CO_2 for 1.5 hours. Scale bars 5 μm and 0.5 μm for middle and left images, respectively.

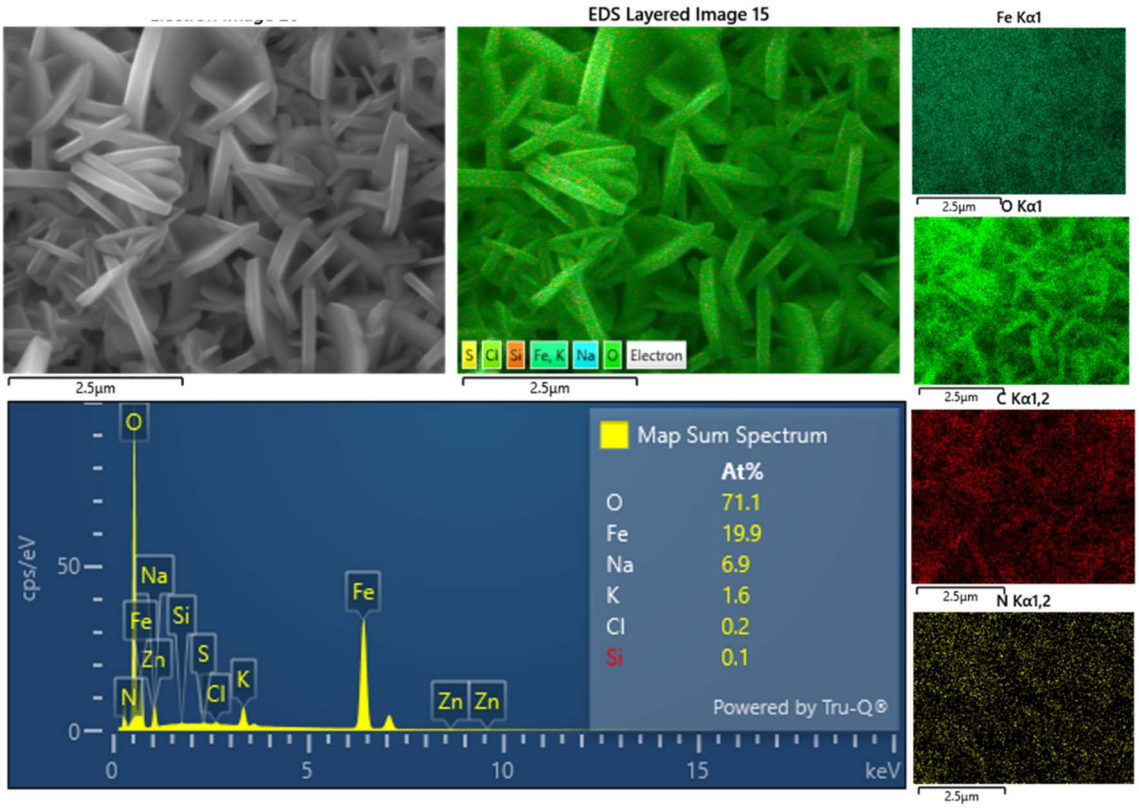

Fig. 13 EDX elemental mapping conducted on the ε-Fe_2N/graphite catalyst electrode after being conditioned at −0.7 V *vs.* RHE in a 0.1 M $NaHCO_3$ solution saturated with CO_2 for 1.5 hours.

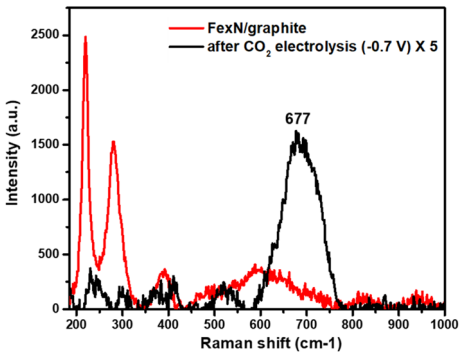

Fig. 14 Raman spectra recorded on an as-prepared ε-Fe_2N/graphite electrode (red trace) and the same electrode after being conditioned at −0.7 V *vs.* RHE for 1.5 hours in a 0.1 M $NaHCO_3$ electrolyte solution saturated with CO_2 (black trace). Excitation was provided by employing a 532 nm laser.

placed at a distance of 200 mm from the samples. This set-up allowed to collect 2D diffraction patterns in transmission geometry from 2 to 45° (2θ) in a single exposure. The samples were all loaded in Lindemann borosilicate capillaries (0.5 mm in diameter) sealed under Ar atmosphere and data collected for 1, 10 or 60 min. The Fit2D program[62] was used for the integration of 2D images into 1D patterns after a calibration using a LaB6 standard crystalline sample. All diffractograms treatments (background removal, peaks search, and profile refinement) have been done with the aid of the Highscore+ software. The Rietveld refinement has been performed with Highscore+ as well. We used a polynomial function to fit the background, and the pseudo-Voigt function has been used for the full profile matching. During Rietveld refinement, when the thermal motions of the four atoms are released, it is interesting to note that the thermal motion of the N3 atom is stronger than the one of the other atoms. This indicates that N3 does not have 100% occupancy, but rather a lower occupancy. This behavior was observed in all refinements performed. This occupancy rate fluctuates between 0.91 and 0.98 depending on the samples. If it is not easy to decide with the Rietveld refinement between 0.91 and 0.98 (data collected on a laboratory diffractometer, without Kalpha1 device, which makes the Full Profile Matching correct but not excellent, and with a low resolution of the first peak of the diffractogram (1 0 1)), it seemed more reasonable to refine this occupancy rate from the cell parameters and the Vegard law. Indeed, for the determination of the cell parameters, only the positions of the peaks are taken into account, and the parameters obtained present good uncertainty values (esd). *Small Angle X-ray Scattering (SAXS) measurements* were performed using an XEUSS 2.0 (Xenocs) small-angle X-ray scattering instrument, equipped with a Pilatus1M (Dectris) detector and a monochromatic X-ray source operating at 8 keV ($\lambda = 1.54$ Å). The X-ray beam measured 0.5 × 0.5 mm in size and had an intensity of 23 million photons per second. Samples were placed in 1.5 mm diameter quartz capillaries and exposed to the beam for 6 × 600 seconds each. A reference based on the scattering from an empty capillary was

subtracted from the SAXS data of the samples. The sample-to-detector distance was set at 1230 mm, and a small beamstop was employed to block the direct beam. This configuration allowed for coverage of a scattering angle range from 0.007 to 0.5 $Å^{-1}$. Due to the isotropy of the scattering images, a radial integration over $\Psi = 360°$ was performed for each dataset to produce a one-dimensional curve representing the intensity $I(q)$ as a function of the scattering vector q ($q = 4\pi \sin\theta/\lambda$, expressed in $Å^{-1}$). The resulting data were processed using the SASVIEW software,[63] which provides a library of form and structure factors for data analysis. Inductively Coupled Plasma Atomic Emission Spectroscopy (ICP-AES) data were obtained after digestion of the powders in aqua regia (a mixture of hydrochloric acid and nitric acid in a 4 : 2 volume ratio), and dilution in milliQ water (18.2 MΩ, pH = 6.5–7) on a ICAP 6300 from ThermoScientific. 2C, H, N elemental analyses were performed on a Thermo Scientific ICAP7600 ICP-OES analyzer and a PerkinElmer 2400 Series II from Thermo Scientific. *Raman spectra* were collected on the powder deposited on a Kapton film. It was measured on an INVIA Raman microspectrometer (RENEISHAW). Excitation was achieved with a 532 nm laser line focused on the sample with a microscope objective (×20), a power of 2.6 mW, $W = 10\%$ and acquisition time = 40 s (4 scans). Raman spectra of sample deposited on FTO electrode were collected on a Raman spectrophotometer (Horiba LabRAM, HR evolution, Vietnam) with 532 nm laser irradiation in the range 100 – 2000 cm^{-1}, neutral density (ND) filter 10.0%. *Magnetic measurements* were conducted using a Quantum Design MPMS5 magnetometer. Samples were prepared in gelatin capsules under argon atmosphere. All data from the magnetic measurements were standardized against the Fe content present in the samples (as determined from ICP-AES analysis). *Mössbauer* spectra were collected on a constant-acceleration spectrometer with a 0.385 GBq source of ^{57}Co (Rh matrix) at 80 K, using an OXFORD cryostat. The thermal scanning was monitored by a temperature controller LAKESHORE 335. The absorber was a sample of about 100 mg of powder that was enclosed in a 20 mm diameter cylindrical plastic sample holder. Mössbauer parameters were fitted to a Lorentzian model using the Recoil software. The isomer shift values are given with respect to metallic iron at room temperature. *For XPS analysis*, the photoelectron emission spectra were recorded using a monochromatised Al Kα ($h\nu$ = 1486.6 eV) source on a ThermoScientific K-Alpha system. The X-ray Spot size was about 400 μm. The Pass energy was fixed at 30 eV with a step of 0.1 eV for core levels and 100 eV for surveys with a step of 1 eV. The spectrometer energy calibration was done using the Au $4f_{7/2}$ (83.9 ± 0.1 eV) and Cu $2p_{3/2}$ (932.8 ± 0.1 eV) photoelectron lines. XPS spectra were recorded in direct mode N (Ec) and the background signal was removed using the Shirley method. The flood gun was used to neutralize charge effects on the top surface.

3.2. Samples preparation

ZVFeNPs were prepared according to already published procedure.[37]

3.2.1. Nitridation of ZVFeNPs in the powder form (samples N1, N2, N3). Typically, 20 mg of ZVFeNPs were placed in an airtight quartz tube resistant to high temperatures within a glovebox. The tube was subsequently positioned in an oven and connected to a device that facilitated the introduction of a gas or mixture of gas flows. Temperature was monitored thanks to a thermocouple located close to the quartz-tube and gas flows were controlled with mass flow controllers. An ammonia trap was installed at the end of the gas circuit. The temperature was increased from room temperature to 200 °C in 20/30 minutes under a hydrogen/argon mixture (respectively 200 mL min^{-1} and 500 mL min^{-1}), then a hydrogen/argon mixture (respectively 200 mL min^{-1} and 200 mL min^{-1}) was maintained for 1 hour at 200 °C, then ammonia (500 mL min^{-1}) was flowed for 5 hours at 200 °C. The sample was cooled down to 100 °C in *ca* 20 min under argon flow (500 mL min^{-1}) then to room temperature in static conditions. The nanomaterial formed (**Sample N**) was then recovered in a glove box and analyzed. Samples N2 and N3: Identical protocol for reproducibility assessment.

3.2.2. Nitridation of ZVFeNPs as thin films on FTO electrodes. 3.4 mg of ZVFeNPs were dispersed in toluene (1 mL) in the presence of 1 μL oleic acid (OA). This mixture was sonicated for 1 hour (ultrasonic bath Fisher Scientific Trans Sonic T460) to ensure thorough dispersion of the NPs. 80 μL of this suspension was then drop casted onto the FTO electrodes and maintained at 50–60 °C to ease the drying process. Subsequently, the electrodes were placed in a quartz tube, as described earlier for the powder, and the same nitridation process as for **Sample N** was applied. The sample were denoted as Fe_2N/FTO.

3.3. The electrochemical analysis

3.3.1. OER. The study was performed using a three-electrode system, consisting of a working electrode (WE), a counter electrode (CE), and a reference electrode (RE), with a BioLogic potentiostat SP-50 (Auvergne-Rhone-Alpes, France). The counter electrode was a platinum mesh (10 × 10 mm). The reference electrode was an Ag/AgCl/KCl 3 M electrode, which was calibrated daily *via* a Cyclic Voltammetry (CV) scan in a $[Fe(CN)_6]^{4-}/[Fe(CN)_6]^{3-}$ 1 M solution, ranging from 0.7 V to −0.2 V *vs.* reference electrode. To prepare calibrating solutions, dissolved $K_3[Fe(CN)_6]$ and $K_4[Fe(CN)_6]$ in 0.1 M phosphate buffer pH = 7.13 (KPi7). Potentials against the reversible hydrogen electrode (RHE) were used throughout the study and calculated according to the well-known equation (eqn (1)):

$$E\,(\text{V } vs.\ \text{RHE}) = E\ vs.\ \text{Ag/AgCl/KCl} + E\text{Ag/AgCl/KCl} + 0.059 \times \text{pH} \quad (1)$$

The potential of the reference electrode was 0.193 ± 0.004 V *vs.* RHE.

Sample Fe_2N/FTO was used as WE.

The catalytic activity was assessed in alkaline (1.0 M KOH, pH = 13.75) media.

3.3.2. CO_2 reduction. Electrolysis test were carried out in a custom two-compartment cell separated by a ceramic membrane (H-cell), in CO_2 saturated 0.1 $NaHCO_3$ (pH 6.8). A Biologic SP-300 potentiostat was used in a three-electrode configuration with Ag/AgCl/KCl 3 M as reference electrode (calibrated as above), Pt mesh as counter electrode, and a modified graphite electrode having a working area of 0.283 cm^2 as the WE. The WE was prepared as follows: a catalyst ink

was fabricated by mixing 3 mg of the Fe_2N nanoparticles powder with a solvent mixture of DI/EtOH (v/v = 80/20), and 5 μl of Nafion 117 solution (5% in alcohol and water). Then 20 μl of the catalyst ink was drop-casted on the surface of the graphite electrode, which was subsequently dried in ambient air at 60 °C for 2–3 hours prior to electrochemical analyses. The catalyst loading was ~0.21 mg cm^{-2}.

The CO_2 reduction reaction test typically comprised two steps: (1) a linear sweep voltammetry (LSV) step from open circuit potential (OCP) to −1.1 V *vs.* RHE and (2) a chronoamperometry (CA) step with increasing reductive potential between −0.7 V and −1.1 V at 0.1 V intervals holding each potential for 1.5 hours. Representative behavior is displayed in Fig. 10.

The gas products were quantified by a PerkinElmer Clarus 690 gas chromatography (GC) system using Ar as a carrier gas with gas flow set at 20 mL min^{-1}. The gas chromatography is equipped with two columns- HayeSepS (1 mm ID, Restek) and molecular sieve MS5a column (1 mm ID, Restek) – as well as two detectors – Thermal conductivity detector (TCD) and flame ionization detector (FID). The TCD and FID detector were operated at 200 °C and 400 °C, respectively. After the electrolysis, 100 μl of the gas in the headspace of the cathode compartment was collected by a gas – tight glass syringe and injected into GC. The faradaic efficiency (FE) was calculated according to eqn (2).

$$\text{FE } (\%) = \frac{Q_{\text{product}}}{Q_{\text{total}}} \times 100\% = \frac{N \times n \times F}{Q_{\text{total}}} \times 100\% \quad (2)$$

with: N = number of moles of product formed during electrochemical CO_2 reduction reaction. n = number of moles of electron required for 1 mole of product formation. F = Faraday constant (96 485 C mol^{-1}).

The quantification of liquid products (formate and acetate) was performed post-electrolysis by using a Dionex Intergrion ion chromatography (IC) system. Deionized water (DI) was used as the mobile phase with a flow rate of 1 mL min^{-1}. The calibration curve was constructed using Sigma-Aldrich formate and acetate standards (1000 ppm). Formate and acetate faradaic efficiency were determined based on the experimentally determined formate concentration [$HCOO^-$], acetate concentration [CH_3COO^-], the total amount of charge passed (q) and the total volume of electrolyte ($V_{\text{electrolyte}}$), as shown in eqn (3).

$$\text{FE } (\%)\text{formate} = \frac{[\text{formate}] \times V_{\text{electroyte}} \times 2 \times F}{q} \quad (3)$$

4. Conclusion

Nanostructured ε-Fe_2N powders and thin films have been prepared from organometallic ZVFeNPs. The conditions used for their nitridation are milder than previously reported,[36] which allowed retaining their initial morphology. This work highlights the advantage of our synthetic approach, namely starting from small ZVFeNPs (below 15 nm), reactive enough towards NH_3, to achieve an iron nitride nanomaterial whose preparation usually requires more steps and drastic conditions. This synthesis strategy opens a new route towards well defined Fe nitride nanomaterials that could find applications in many fields such as energy storage or catalysis. We have shown that this synthetic approach could be efficiently used to produce thin layers of iron nitride NPs on conductive supports for application in electrocatalysis.

The ε-Fe_2N thin film grown on a fluorine doped tin oxide (FTO) electrode showed an honorable catalytic activity for the oxygen evolution reaction in an alkaline medium, with an onset overpotential of 320 mV and a small Tafel slope of 57.8 mV per decade. The ε-Fe_2N catalyst was found to experience an activation process, namely the electrochemical oxidation of surface ε-Fe_2N generating iron oxide species prior to reach its highest catalytic performance. The actual catalyst for the OER would be described as core–shell $Fe_2N@FeO_x$. This activation did not cause any significant change in the initial morphology of ε-Fe_2N NPs. In the stark contrast, a significant morphological change was observed, accompanied by an obvious chemical change, when employing ε-Fe_2N NPs as a catalyst for the CO_2RR. As such, FeO_x nanoflakes were generated and co-existed with spherical NPs after the CO_2 reduction catalysis. Even though, the CO_2RR was still less favorable than the HER on the ε-Fe_2N NPs catalyst, this work demonstrates for the first time the CO_2 reduction catalytic ability and selectivity of the iron nitride. Further works should require to elucidate the nature of the catalytic sites as well as to reveal the reason behind the CO_2-to-acetate production selectivity. In this respect, the good NP morphology control afforded by our synthetic approach will ease mechanistic studies, possibly allowing modeling of the reaction intermediates.

Author contributions

Conceptualization – CA, MR, PDT; data curation – AE, QTN, PR, LV, DNG, VTT, LTL, JE; formal analysis – AE, PR, LV, JE; funding acquisition – MR, CA, PDT; investigation – AE, QTN, PR, LV; project administration – CA; resources – FD; supervision – CA, MR, PDT; validation – AE, QTN, JE; visualization –AE, MR, CA, QTN; writing – original draft – CA, MR, QTN, PDT; writing – review & editing – all.

Conflicts of interest

There are no conflicts to declare.

Data availability

The data supporting this article have been included as part of the supplementary information (SI). Supplementary information is available. See DOI: https://doi.org/10.1039/d5ra08111d.

Acknowledgements

We thank Université de Toulouse – UPS, CNRS, INSA and ANR (project ANR-19-ASTR-0021-03) for financial support, UAR Castaing for the access to electron microscopes and ICT for the access to its characterization platforms. Quyen T. Nguyen and

Phong D. Tran acknowledge the Vietnam Academy of Science and Technology for funding support through the project THTETN.04/23-24. We thank J.F. Meunier for recording the Mössbauer spectra, M. Tasse for recording Raman spectra and S. Pinaud for his help in the nitridation process. We thank B. Baptiste for the diffraction experiments performed at the X-ray diffraction platform of the Institut de Minéralogie, de Physique des Matériaux et Cosmochimie (IMPMC), Sorbonne Université (Paris, France). The authors would also like to thank the Federation FERMAT for their assistance with SAXS measurements. This work benefited from the use of the SasView application, originally developed under NSF Award DMR – 0520547. SasView also contains code developed with funding from the EU Horizon 2020 programme under the SINE2020 project Grant No. 654000. AE thanks Région Occitanie and INSA (AIME project No. 00137767/22009565) for her PhD grant.

Notes and references

1 X. Liang, C. Wang, M. Yu, S. Liu, Y. Zhang and S. Zhong, *J. Mater. Sci.: Mater. Electron.*, 2023, **34**, 31.
2 J. Ren, L. Zhang, N. Bao, X. Fan and H. Yang, *J. Electron. Mater.*, 2022, **51**, 966–977.
3 J.-P. Wang, *J. Magn. Magn. Mater.*, 2020, **497**, 165962.
4 M. Mekata, H. Yoshimura and H. Takaki, *J. Phys. Soc. Jpn.*, 1972, **33**, 62–69.
5 I. Dirba, C. K. Chandra, Y. Ablets, J. Kohout, T. Kmječ, O. Kaman and O. Gutfleisch, *J. Phys. D: Appl. Phys.*, 2022, **56**, 025001.
6 Y. Ablets, O. Gutfleisch and I. Dirba, *Int. J. Mag. Part Imag.*, 2023, **9**, 572.
7 Y. Zhang, Y. Xie, Y. Zhou, X. Wang and K. Pan, *J. Mater. Res.*, 2017, **32**, 1770–1776.
8 X. Zeng, S. M. Choi, Y. Bai, M. J. Jang, R. Yu, H.-S. Cho, C.-H. Kim, N. V. Myung and Y. Yin, *ACS Appl. Energy Mater.*, 2020, **3**, 146–151.
9 Y. Wang, M. Zhu, G. Wang, B. Dai, F. Yu, Z. Tian and X. Guo, *Nanomaterials*, 2017, **7**, 404.
10 J. Xiao, Y. Xu, Y. Xia, J. Xi and S. Wang, *Nano Energy*, 2016, **24**, 121–129.
11 Y. Lou, J. Liu, M. Liu and F. Wang, *ACS Catal.*, 2020, **10**, 2443–2451.
12 G. Lei, J. Wu, L. Qin, S. Wu, F. Zhang, X. Fan, W. Peng and Y. Li, *Int. J. Hydrogen Energy*, 2024, **58**, 1088–1097.
13 M. Sajjad, J. Zhang, Z. Mao and Z. Chen, *J. Alloys Compd.*, 2024, **976**, 172626.
14 M. Wang, L. Zhang, Y. He and H. Zhu, *J. Mater. Chem. A*, 2021, **9**, 5320–5363.
15 F. Song, L. Bai, A. Moysiadou, S. Lee, C. Hu, L. Liardet and X. Hu, *J. Am. Chem. Soc.*, 2018, **140**, 7748–7759.
16 Y. Lee, W. Jeong, Y. J. Hwang, B. An, H. Lee, H. Jeong, G. Kim, Y. Park, M. Kim and D.-H. Ha, *J. Mater. Chem. A*, 2024, **12**, 28574–28594.
17 X. Peng, C. Pi, X. Zhang, S. Li, K. Huo and P. K. Chu, *Sustainable Energy Fuels*, 2019, **3**, 366–381.
18 F. Yu, H. Zhou, Z. Zhu, J. Sun, R. He, J. Bao, S. Chen and Z. Ren, *ACS Catal.*, 2017, **7**, 2052–2057.
19 W. Wang, L. Liu, W. C. Leng, L. L. Cui and Y. Gong, *Inorg. Chem.*, 2021, **60**, 12136–12150.
20 S. Nitopi, E. Bertheussen, S. B. Scott, X. Liu, A. K. Engstfeld, S. Horch, B. Seger, I. E. L. Stephens, K. Chan, C. Hahn, J. K. Nørskov, T. F. Jaramillo and I. Chorkendorff, *Chem. Rev.*, 2019, **119**, 7610–7672.
21 A. G. Yohannes, C. Lee, P. Talebi, D. H. Mok, M. Karamad, S. Back and S. Siahrostami, *ACS Catal.*, 2023, **13**, 9007–9017.
22 C.-W. Tsai, M.-H. Tu, C.-J. Chen, T.-F. Hung, R.-S. Liu, W.-R. Liu, M.-Y. Lo, Y.-M. Peng, L. Zhang, J. Zhang, D.-S. Shy and X.-K. Xing, *RSC Adv.*, 2011, **1**, 1349–1357.
23 W. Sun, C. Liu, Y. Li, S. Luo, S. Liu, X. Hong, K. Xie, Y. Liu, X. Tan and C. Zheng, *ACS Nano*, 2019, **13**, 12137–12147.
24 H. Jiang, L. Huang, Y. Wei, B. Wang, H. Wu, Y. Zhang, H. Liu and S. Dou, *Nano-Micro Lett.*, 2019, **11**, 56.
25 X. Cui, X. Liang, J. Chen, W. Gu, G. Ji and Y. Du, *Carbon*, 2020, **156**, 49–57.
26 M. Idrees, A. S. Haidyrah, A. ur-Rehman, Q. Zhang, X. Li and S. M. Abbas, *J. Alloys Compd.*, 2021, **883**, 160824.
27 M. Wang, Y. Yang, X. Liu, Z. Pu, Z. Kou, P. Zhu and S. Mu, *Nanoscale*, 2017, **9**, 7641–7649.
28 N. Zhang, S. Xie, W. Wang, D. Xie, D. Zhu and F. Cheng, *J. Electrochem. Soc.*, 2020, **167**, 20505.
29 M.-S. Balogun, M. Yu, Y. Huang, C. Li, P. Fang, Y. Liu, X. Lu and Y. Tong, *Nano Energy*, 2015, **11**, 348–355.
30 Y. Hu, H. Yang, M.-S. Balogun and J. Chen, *Inorg. Chem. Commun.*, 2023, **153**, 110744.
31 B. Lei, J. Wen, S. Ren, L. Zhang and H. Zhang, *New J. Chem.*, 2019, **43**, 18277–18284.
32 D. Moszynski, I. Moszynska and W. Arabczyk, *Mater. Lett.*, 2012, **78**, 32–34.
33 D. Moszynski, K. Kielbasa and W. Arabczyk, *Mater. Chem. Phys.*, 2013, **141**, 674.
34 Y. Fujiwara, J.-S. M. Lee, M. Tsujimoto, K. Kongpatpanich, T. Pila, K. Iimura, N. Tobori, S. Kitagawa and S. Horike, *Chem. Mater.*, 2018, **30**, 1830–1834.
35 J. Choi and E. G. Gillan, *Inorg. Chem.*, 2009, **48**, 4470–4477.
36 S. Bhattacharyya, *J. Phys. Chem. C*, 2015, **119**, 1601.
37 F. Dumestre, C. Amiens, B. Chaudret, P. Fejes and P. Renaud, *Science*, 2004, **303**, 821.
38 L.-M. Lacroix, A. Meffre, C. Gatel, P.-F. Fazzini, S. Lachaize, M. Respaud and B. Chaudret, *ChemPlusChem*, 2019, **84**, 302–306.
39 L.-M. Lacroix, S. Lachaize, A. Falqui, M. Respaud and B. Chaudret, *J. Am. Chem. Soc.*, 2009, **131**, 549–557.
40 NanoMePS, *Nanomatériaux et complexes organométalliques*, http://www.nanomeps.fr/, accessed July 21, 2025.
41 V. Kelsen, B. Wendt, S. Werkmeister, K. Junge, M. Beller and B. Chaudret, *Chem. Commun.*, 2013, **49**, 3416.
42 A. Meffre, B. Mehdaoui, V. Kelsen, P. F. Fazzini, J. Carrey, S. Lachaize, M. Respaud and B. Chaudret, *Nano Lett.*, 2012, **11**, 5128–5134.
43 B. Hammouda, *J. Appl. Crystallogr.*, 2010, **43**, 716–719.
44 B. Hammouda, *J. Appl. Crystallogr.*, 2010, **43**, 1474–1478.
45 T. Varga, L. Vásárhelyi, G. Ballai, H. Haspel, A. Oszkó, Á. Kukovecz and Z. Kónya, *ACS Omega*, 2019, **4**, 130–139.

46 E. H. D. M. van Voorthuysen, D. O. Boerma and N. C. Chechenin, *Metall. Mater. Trans. A*, 2002, **33**, 2593–2598.
47 M. A. J. Somers, B. J. Kooi, L. Maldzinski, E. J. Mittemeijer, A. A. Van Der Horst, A. M. Van Der Kraan and N. M. Van Der Pers, *Acta Mater.*, 1997, **45**, 2013–2025.
48 M. Minagawa, H. Yanagihara, M. Kishimoto and E. Kita, *Mater. Trans.*, 2010, **51**, 2173–2176.
49 T. Hinomura and S. Nasu, *Hyperfine Interact.*, 1998, **111**, 221–226.
50 H. Nakagawa, S. Nasu, H. Fujii, M. Takahashi and F. Kanamaru, *Hyperfine Interact.*, 1992, **69**, 455–458.
51 M. Kano, T. Nakagawa, T. A. Yamamoto and M. Katsura, *J. Alloys Compd.*, 2001, **327**, 43–46.
52 V. Ashok, A. Gayathri, M. Vijayarangan and J. Jayabharathi, *Sustainable Energy Fuels*, 2024, **8**, 3452–3464.
53 X. Huang, Z. Yang, B. Dong, Y. Wang, T. Tang and Y. Hou, *Nanoscale*, 2017, **9**, 8102–8106.
54 W. Wang, L. Liu, W. C. Leng, L. L. Cui and Y. Gong, *Inorg. Chem.*, 2021, **60**, 12136–12150.
55 M. V. Abrashev, V. G. Ivanov, B. S. Stefanov, N. D. Todorov, J. Rosell and V. Skumryev, *J. Appl. Phys.*, 2020, **127**, 205108.
56 F. Bressan, R. L. Hess, P. Sgarbossa and R. Bertani, *Heritage*, 2019, **2**, 1551–1587.
57 F. Yu, H. Zhou, Z. Zhu, J. Sun, R. He, J. Bao, S. Chen and Z. Ren, *ACS Catal.*, 2017, **7**, 2052–2057.
58 P. Chen, K. Xu, Z. Fang, Y. Tong, J. Wu, X. Lu, X. Peng, H. Ding, C. Wu and Y. Xie, *Angew. Chem.*, 2015, **127**, 14923–14927.
59 Y. Hu, D. Huang, J. Zhang, Y. Huang, M. -Sadeeq, J. T. Balogun and Y. Tong, *ChemCatChem*, 2019, **11**, 6051–6060.
60 O. N. Shebanova and P. Lazor, *J. Solid State Chem.*, 2003, **174**, 424–430.
61 A. P. Grosvenor, B. A. Kobe, M. C. Biesinger and N. S. McIntyre, *Surf. Interface Anal.*, 2004, **36**, 1564–1574.
62 A. P. Hammersley, *J. Appl. Crystallogr.*, 2016, **49**, 646–652.
63 M. Doucet, J. H. Cho, G. Alina, Z. Attala, J. Bakker, W. Bouwman, R. Bourne, P. Butler, I. Cadwallader-Jones, K. Campbell, T. Cooper-Benun, C. Durniak, L. Forster, P. Gilbert, M. Gonzalez, R. Heenan, A. Jackson, S. King, P. Kienzle, J. Krzywon, B. Maranville, R. Murphy, T. Nielsen, L. O'Driscoll, W. Potrzebowski, S. Prescott, R. Ferraz Leal, P. Rozyczko, T. Snow, A. Washington and C. Wolf, SasView version 5.0.5, Zenodo, 2022, DOI: 10.5281/ZENODO.6331344.